FR 8203219

Université Scientifique et Médicale de Grenoble

INSTITUT DES SCIENCES NUCLÉAIRES DE GRENOBLE

53, avenue des Martyrs – GRENOBLE

ISN 82.12
March 1982

FUSION AND DEEPLY INELASTIC COLLISIONS OF ^{20}Ne WITH ^{27}Al

NGUYEN VAN SEN, R. DARVES-BLANC, J.C. GONDRAND, F. MERCHEZ.

Submitted for publication

Laboratoire associé à l'Institut National de Physique Nucléaire et de Physique des Particules.

39 pages

FUSION AND DEEPLY INELASTIC COLLISIONS OF ^{20}Ne WITH ^{27}Al

Nguyen Van Sen, R. Darves-Blanc, J.C. Gondrand

and F. Merchez

Institut des Sciences Nucléaires, IN2P3 and USMG,

38026 Grenoble, France

Fusion cross sections were measured for ^{20}Ne bombardments of ^{27}Al from 32 to 151 MeV by detecting the evaporation residues from the compound nucleus decay with gas counter telescopes. Charge, energy, and angular distributions of projectilelike fragments from the deeply inelastic collisions were also measured at 151 MeV. The fusion excitation function was analyzed through the barrier penetration model and compared to the predictions of the statistical yrast line model. The critical angular momentum and the grazing one deduced from the fusion and elastic scattering data were used in the interpretation of the kinetic energies of the deeply inelastic fragments in terms of a rotating dinuclear model.

NUCLEAR REACTIONS $^{20}Ne + ^{27}Al$, E = 32.5 to 151 MeV ; measured evaporation residue $\sigma(E,\theta)$; deduced $\sigma(E)$ total fusion excitation function ; barrier and critical parameters. E = 55.7, 63, 125, 151 MeV ; measured elastic scattering $\sigma(\theta)$; deduced optical potentials ; reaction cross sections σ_R. E = 151 MeV ; measured charge, energy and angular distributions for $4 \leqslant Z \leqslant 12$ fragments. Natural target. Gas ionization and Si detectors.

I. INTRODUCTION

Complete fusion between complex nuclei has been the subject of many studies.[1-3] In most theoretical approaches the fusion cross sections at energies immediately above the Coulomb barrier were interpreted in terms of barrier penetration models, although promising results were obtained by microscopic calculations based on time-dependent quantum mechanical treatments.[4-6] Using real one-dimensional potentials, a recent comprehensive analysis of up to 87 fusion excitation functions was able to deduce fusion barriers that are only slightly dependent on the model potential.[1] The simple barrier penetration model is, however, inadequate for describing the fusion at higher energies[1,3] where it competes with energy - dissipating processes[7,8] and direct reactions[9-13]; and at subbarrier energies where "dynamic effects"[1] should be taken into account. Even with beam energies lower than 10 MeV/amu, the ^{20}Ne projectiles are well suitable for an experimental study of the evolution of the reaction mechanism from subbarrier fusion to deeply inelastic collisions and fragmentation mechanisms, particularly when medium-mass targets, $A \simeq 27 - 60$, are bombarded with. For example, many aspects of the $^{20}Ne + {}^{40}Ca$ collision in that energy range has been investigated by Nguyen Van Sen et al.,[14-16] Madurga et al.,[17] Fröhlich et al.,[10] and Udagawa et al.[11]

The present work is devoted to the $^{20}Ne + {}^{27}Al$ system. With gas counter telescopes the complete fusion of ^{20}Ne with ^{27}Al has been studied at 138 and 210MeV by Kozub et al.,[18] and 120 MeV by Natowitz et al..[19] Several preliminary data have been reported at 60-290 MeV by Bohne et al.[20] using a time-of-flight system. Earlier data obtained by Kowalski et al.[21] at 87, 140 and 198 MeV with mica track detectors differ considerably from the more recent results.[18] The fusion data for the $^{20}Ne + {}^{27}Al$ system, however, are still scarce compared to those for $^{16}O + {}^{27}Al$.[16,22-26] The measurements for this system have shown that notable discrepancies occurred between data from independent experiments and that many experiments are useful, even necessary for a reliable assessment of the fusion cross section excitation curve. Thus, although a large body of fusion data is available for various systems,[1] it is still worth to concentrate experimental efforts on some typical systems.

Measurements of the complete fusion cross section of ^{20}Ne with ^{27}Al were performed in the present work at 32.5, 41.5, 50, 55.7, 63, 70, 100 and 151 MeV using gas counter telescopes. The data associated to previous results[18-20] were analyzed in terms of a barrier penetration model. The fusion barrier parameters deduced were compared to those obtained from an optical model analysis of the elastic scattering angular distributions that were measured at 55.7, 63, 125, and 151 MeV by means of Si detectors. The critical parameters[27,28] were deduced from the higher energy data, which were also compared to the predictions of the statistical yrast model.[29] This simple model provided in a recent analysis by Lee et al.[29] a good description of almost all existing fusion cross sections for compound systems up to $A = 80$.

Medium-weight targets used in previous studies of deeply inelastic collisions induced by ^{20}Ne include ^{27}Al at 120 MeV beam energy,[19] ^{40}Ca at 151 MeV,[16] Ni at 164 MeV,[30] ^{63}Cu at 166 MeV,[31] and Cu at 170 and 252 MeV.[32] The data are fairly illustrative of the concept of a rotating dinuclear complex which separates into projectile-and target-like fragments. In the present work the angular distributions of the projectile-like fragments produced by the ^{20}Ne + ^{27}Al collision at 151 MeV were measured with an ionization chamber. The critical angular momentum and the grazing one deduced from the fusion and elastic scattering data were used in an interpretation of the fragment kinetic energies in terms of a rotating dinuclear system whose contributing initial angular momentum depends explicitly on the amount of nucleon transfer.[16,33]

II. EXPERIMENTAL PROCEDURE

The experiments were carried out using ^{20}Ne beams from the Grenoble isochronous cyclotron. Self-supporting natural Al targets were placed at the center of a 1m diam. scattering chamber. Thicknesses of 50 - 100 $\mu g/cm^2$ were used for the fusion measurements and of 200 - 500 $\mu g/cm^2$ for the deeply inelastic reaction measurements. The targets were always protected from oxidation by vacuum or argon atmosphere. A collimator composed of three successive tantalum slits limited the focused beam spot at the target position to about 3 mm in diameter. Beam intensities up to 100 electric nA were collected during the measurements by a Faraday cup placed downstream of the scattering chamber.

The fusion cross sections for 30 - 100 MeV incident energies were measured by detecting the evaporation residues with a gas-flow proportional counter having a low resistivity Si detector on its internal rear side; this counter has been described previously.[15] The experiments at 151 MeV were performed with an ionization chamber described elsewhere.[16] Both counters were run with a mixture of 90% Ar + 10% CH_4 gas at constant pressures. Low pressures corresponding to about 200 $\mu g/cm^2$ ΔE gas detector were used for the detection of the heavy evaporation residues, instead of pressures about four times higher for the projectilelike fragments produced by the deeply inelastic collisions. The solid-angles sustained by the ΔE gas counters were limited to about 0.1 msr, allowing accurate measurements at the small forward angles, whereas the sensitive area of the E solid detectors were chosen to be large enough to take into account the multiple scattering of some heavy fragments on the ΔE-detector gas.

Two Si monitor detectors were placed at fixed forward angles in order to obtain the relative normalization of the fragment yield detected by the gas counter, and to control the beam centering on the target. The absolute normalization of the cross section was obtained by comparing the fragment yield to the elastic counts within the same $E - \Delta E$ combination. The accuracy of the elastic cross section measured by the gas counters was checked at 55.7, 63, 125 and 151 MeV by comparing the results to the angular distributions that were independently measured using solid-state detectors with the same experimental set-up as in Ref.[14]. The consistency between the fusion measurements made with the proportional counter and with the ionization chamber was checked by comparing their data at 63 MeV. The overall features of the E vs. ΔE spectra at 151 MeV are similar to those shown by Natowitz et al.[19] in their study of the $^{20}Ne + ^{27}Al$ system at 120 MeV.

The experimental procedure for obtaining the fusion and deeply inelastic elemental yields, energy spectra, and cross section has been described in detail[15,16]. Two typical elemental yields are plotted in Fig. 1. The upper part shows the charge distribution of the projectilelike fragments detected at 14° and 151 MeV incident energy, the elastic scattering peak being discarded. The charge resolution obtained is about $\Delta Z = 0.3$. The lower part in Fig.1 shows the charge distribution obtained at 63 MeV and 10° by running the gas counter at low pressure. The charge resolution is then about $\Delta Z = 1$, sufficient to separate the evaporation residues with $16 \leq Z \leq 25$ from the lighter fragments produced mostly by the large elastic scattering yield, the background and some small contributions from the fusion of the ^{20}Ne projectiles with C and O contaminants.

III. EXPERIMENTAL RESULTS

The fusion angular distributions were measured from 4° to an angle where the contribution of the yield to the angle-integrated cross section σ_{fus} is negligible. In order to obtain σ_{fus}, the angular distribution was extrapolated into the 0° - 4° region not measured by fitting the data in the range 0° - 8° with the equation[15]

$$d\sigma_{fus} / d\Omega = a \sin^2 \theta + b \qquad (1)$$

The σ_{fus} was actually deduced by finding the area under the curve $d\sigma_{fus}/d\theta$ vs. θ, so that the uncertainty due to the extrapolation procedure does not exceed a few percent. Some typical $d\sigma_{fus}/d\theta$ angular distributions are shown in Fig. 2. The general pattern is similar to that observed for other systems. The integrated cross section σ_{fus} are reported in Table I with errors including the statistical uncertainty, the absolute normalization, and the extrapolation procedure uncertainties. The σ_{fus} are plotted in Fig.3 together with data at 120 MeV from Natowitz et al.[19], at 138 and 210 MeV from Kozub et al.[18], and at 60 - 290 MeV from Bohne et al.[20]. The excitation function has an average trend similar to those obtained for neighboring systems such as $^{16}O + ^{27}Al$,[22-26] in agreement with the Glas-Mosel picture.[28]

The elastic angular distributions measured at 55.7, 63, 125 and 151 MeV are plotted in Fig. 4. The errors are about $\pm$ 5 % including statistical and background substraction uncertainties ($\pm$ 3 %), and absolute normalization errors ($\pm$ 3 %). The angular accuracy is about $\pm$ 0.05° and the ^{20}Ne beam energies are determined with an uncertainty of about 1 MeV. The elastic cross section falls off to $\frac{1}{4}$ of the Rutherford value at 52.7°, 44.3°, 19° and 16°, respectively. The numerical tabulations of the data can be obtained from the authors.

At 151 MeV, energy spectra were obtained for fragments from Be to Al, in addition to the fusion and elastic scattering measurements. Most spectra present a bell-shaped distribution corresponding to a strongly damped process. At backward angles and/or for the fragments far from the projectile these distributions are nearly symmetric, and their width is practically independent of the fragment detected. But for the fragments near the projectile, the distributions at forward angles are broader and more asymmetric with a longer low-energy tail. Some typical spectra are shown in Fig. 5. At angle forward of the grazing angle a bell shaped structure could not be clearly observed for the Ne fragment because of the elastic scattering yield, the low-energy background, and the increasing contribution from inelastic scatterings and quasielastic components, and also of the decreasing energy separation between the elastic peak and the strongly damped component. For fragments with $Z \geqslant 12$ the evaporation residues give rise to a low energy component which superposes on and progressively dominates the deeply inelastic component at forward angle.

The elemental yields deduced from the bell-shaped part of the fragment spectra present a clear odd-even effect in function of the fragment charge, as illustrated in Fig. 1. This effect also observed in other systems, is partly attributable to particle decays from the excited primary fragments favoring the formation of final even-charge products[31]. The variance of the charge distribution decreases at forward angle where the yields of the fragments near the projectile are strongly dominant, similarly to previous results.[16,19,30-32]

The elemental angular distributions displayed in Fig. 6 are more and more forward-peaking when the transferred nucleon number decreases. Those for Be, B and Mg are fairly close to the dashed curves corresponding to a $1 / \sin\theta_{c.m.}$ angular distribution. The angular behaviour of the total kinetic energy E_F calculated for the centroid of the bell-shaped structure using two-body kinematics is shown in Fig. 7. For fragments far from the projectile E_F is nearly independent of angle while for the other fragments, for example N and O, E_F decreases as the angle increases up to about 30°, and then keeps a nearly constant value beyond this angle. The overall features of the elemental cross section and of the total kinetic energy suggest a fully relaxed process for the production of Be, B, and Mg. Such a mechanism is also present for the other fragments, but it should compete, particularly at forward angles, with a fast interaction time process, although the data for ^{20}Ne + ^{27}Al are somewhat less illustrative of such a competition than for slightly heavier systems[16].

The total elemental yields were obtained by integrating over angle the $d\sigma/d\theta_{lab}$ deduced from the angular distributions in Fig. 6. The $d\sigma/d\theta_{lab}$ data were extrapolated into the forward angular range not measured by a smooth hand-drawn continuation. For the Ne fragment, the data at angles less than 10° were tentatively obtained by interpolation between the distributions for F and Na ; such an interpolation is assumed in light of the forward angle distribution similarity for those fragments. The angle-integrated elemental yields are reported in Table II where the error bars take into account the statistics uncertainty and the extrapolation procedure errors. The cross sections so obtained actually include some contributions from the quasielastic collisions particularly at forward angles where the deeply inelastic component cannot be unambiguously resolved from the quasielastic component. The contributions from the fission of the ^{47}V compound nucleus are expected to be negligible since the fission barrier predicted by the liquid-drop model[34,35] vanishes at a relatively high angular momentum[3], $l \simeq 46\hbar$ compared to the fusion critical angular momentum deduced from the data with the sharp-cutoff approximation, and reported in Table I.

IV. THEORETICAL ANALYSIS

A - Elastic scattering

The elastic angular distributions measured at 55.7, 63, 125 and 151 MeV were analyzed in terms of the optical model. Calculations were performed with the SPI code[36] using a four-parameter potential

$$U(r) = V_{Coul} - \frac{(V + iW)}{1 + \exp\left\{\left[r - r_o(A_P^{1/3} + A_T^{1/3})\right] /a\right\}}, \qquad (2)$$

where V_{Coul} is the Coulomb potential for a uniformly charged sphere of the same radius as the complex nuclear part. Since the present measurements were limited to cross sections higher than 10^{-2} times the Rutherford value and a smooth exponential fall-off was observed for the ratio σ/σ_R beyond its maximum as shown in Fig. 4, a four-parameter potential is expected to provide an acceptable description of the data, similarly to previous works.[14-16,37-39] Although measurements of large-angle elastic scattering introduce more empirical constraints on the optical model,[40] the heavy-ion elastic scattering is sensitive only to the surface region of the nuclear potential,[41] so that there is until now no definite receipt to determine unambiguously the potential strength at the interior of the nucleus.

In the present analysis, the real potential strength V is postulated as previously[15,16] to have the value deduced from the liquid drop model by Siwek-Wilczynska and Wilczynski,[42]

$$V = b_{surf}\left[A_P^{2/3} + A_T^{2/3} - (A_P + A_T)^{2/3}\right] , \tag{3}$$

where b_{surf} = 17 MeV is the surface energy parameter. For the $^{20}Ne + {}^{27}Al$ system, V = 56.86 MeV.

The strength V being fixed, a gridding search was made for the imaginary depth W. For a chosen value of W in the range 0 - 57 MeV the χ^2 minimization was performed by adjusting r_o and a. The best fits shown in Fig. 4 was obtained with W = 45 MeV for all the angular distributions considered, and various combinations of r_o and a tabulated in Table III. The energy-averaged radius and diffuseness are consistent with the results obtained for the $^{20}Ne + {}^{40}Ca$ system[15] using Eq.(3) for V.

The experimental elastic scattering cross sections in Fig. 4 fall off to $\frac{1}{4}$ of the Rutherford value at c.m. angles $\theta_{1/4}$ reported in Table III together with the classical grazing angular momenta deduced through the Blair relationship[43]

$$l_{gr} \approx l_{1/4} = \eta \cot (\theta_{1/4} / 2) , \tag{4}$$

where η is the Sommerfeld parameter. The classical total cross section are then

$$\sigma_R^{(1/4)} = \pi \lambda\!\!\!^{-2} (l_{gr} + 1)^2 \tag{5}$$

where $\lambda\!\!\!^{-}$ is the reduced wavelength..

The grazing angular momentum obtained with Eq.(4) are practically equal to the angular momentum for which the optical model transmission coefficient is equal to 0.5, so that the $\sigma_R^{(1/4)}$ calculated through Eq.(5) are well consistent with the optical model total cross section σ_R as reported in Table III.

The height and position of the s-wave interaction barrier, also reported in Table III, will be compared to the fusion barrier parameters in the next section.

B - Fusion

Although promising results have been obtained from microscopic approaches of the fusion process,[4,5] the simple semi-classical model based on the penetration of the nucleus-nucleus potential barrier were so far widely used to deduce the s-wave barrier parameters. Fusion is assumed then the occur when the nucleus-nucleus potential barrier has been passed.[1] Thus the fusion cross section is

$$\sigma_{fus} = \pi \lambda\!\!\!^{-2} \sum_{l} (2l + 1)\, T_l \quad , \qquad (6)$$

where $\lambda\!\!\!^{-}$ is the reduced wavelength, and T_l is the transmission coefficient which may be calculated via the Hill-Wheeler parabolic approximation.[44]

This model is used in the present analysis of the fusion data. For each orbital angular momentum l the nucleus-nucleus potential was assumed to consist of the sum of the point charge Coulomb potential, the centrifugal component, and the nuclear potential.

The nuclear potential may be the real part of the optical potential deduced from the fits of the elastic scattering data. Since the elastic scattering is sensitive to a narrow part of the potential tail around the strong absorption radius while the fusion process is sensitive to closer distances, particularly to the height and the shape of the interaction barrier, a simultaneous fit of the elastic scattering with the optical model and of the fusion data may provide a reliable nuclear potential tail. In fact the reaction theory calculations involving the nuclear potential require generally a potential taking into account explicitly the mass, charge and size of the interacting nuclei. Deducing such a potential would imply an extensive systematic measurement and analysis of the elastic scattering and fusion data. Universal nucleus-nucleus potentials were, instead, deduced by several authors[1] using simple basic assumptions. Vaz et al.[1] have used such potentials in a systematic analysis of 87 fusion excitation curves. In the present work the proximity potential is employed in order to compare the results to those obtained in previous works[15,16] using such a potential.

The proximity potential, derived by Blocki et al.[45] assuming that the nuclear force is short in comparison with nuclear dimensions, is given by

$$V_N(\zeta) = 4\pi\gamma \frac{C_P C_T}{C_P + C_T} b \, \phi(\zeta) \tag{7}$$

where

$$\gamma = 0.9517 \, (1 - 1.7826 \, I^2) \ \mathrm{MeV/fm}^2, \tag{8}$$

$$I = (N_P + N_T - Z_P - Z_T) / (A_P + A_T), \tag{9}$$

C_P, C_T are the half-density nuclear radii for the projectile and the target, respectively, and I is the neutron excess of the total system. The C's are related to the equivalent sharp radii by

$$C_i = R_i \left[1 - \left(\frac{b}{R_i}\right)^2 + \dots \right] , \tag{10}$$

where $b \approx 1$ fm is the surface width, and

$$R_i = r_o A_i^{1/3} - 0.76 + 0.8 \, A_i^{-1/3}, \tag{11}$$

with $r_o = 1.28$ fm.

The function $\phi(\zeta)$ is expressed in terms of the separation distance ζ between the half-density surfaces

$$\zeta = (r - C_P - C_T) / b \tag{12}$$

by means of a universal cubic-exponential formula.[45]

Blocki et al.[45] have suggested that some variation of the proximity potential standard parameters, particularly the nuclear radii, may be necessary in order to take into account the individual nuclear properties of the colliding nuclei. Vaz and Alexander[46] in a systematic analysis of the fusion data have found that small changes in the parameters γ, b, and R are required to give reasonable fits to the experimental data ; variations in γ or b have, however, much smaller effects than in R.

Calculations performed with the proximity potential for $^{20}Ne + ^{27}Al$ provided for the low-energy part of the excitation curve results about 30 % lower than the measured data if $r_o = 1.28$ fm as recommended by Blocki et al[45]. To fit the data, as shown in Fig.3, r_o had to be increased up to $r_o = 1.35$ fm. Such a value is consistent with those deduced from the $^{20}Ne + ^{40}Ca$ and $^{16}O + ^{40}Ca$ data, $r_o = 1.37$ and 1.36 fm, respectively.[15] Moreover the near barrier fusion cross sections of the $^{16}O + ^{27}Al$ [22-26] and $^{19}F + ^{27}Al$ [47] can also be well reproduced with $r_o = 1.35$ fm. These results support a previous observation[15] that there is no significant effect of the large static deformation of the ^{20}Ne projectile on the fusion cross section at energies immediately above the interaction barrier. This deformation leads to an enhancement of the total reaction cross section σ_R by contributions from peripheral reactions, particularly inelastic scatterings, so that σ_{fus} is appreciably smaller than σ_R even at energies not far above the interaction barrier. In the present study on $^{20}Ne + ^{27}Al$, the ratio σ_{fus} / σ_R is about 0.7 in the 40 - 70 MeV lab energy range.

The simple barrier penetration model based on Eq.(6) is generally inadequate for the description of the high energy part of the fusion excitation curve.[1,3] With a proximity potential having $r_o = 1.35$ fm the critical angular momentum l_{cr} for $^{20}Ne + ^{27}Al$, defined as the angular momentum for which the projectile just surmounts the barrier provided by the Coulomb, centrifugal, and nuclear potentials, attains a saturated value, $l_{cr} = 37$, for $E_{lab} \gtrsim 110$ MeV, i.e. no minimum in the total potential energy and then no fusion occurs for partial waves with $l > 37$. The theoretical cross sections calculated with Eq.(6) are then proportionnal to $1/E_{cm}$ as shown in Fig.3, where the data are well fitted up to about $E_{lab} \doteq 150$ MeV.

In fact the average trend of the data is rather in the form

$$\sigma_{fus} = \pi R_j^2 \left(1 - V_j / E_{c.m.} \right)$$

with $R_j = R_B = 1.44\ (20^{1/3} + 27^{1/3})$ fm and $V_j = V_B = 19.21$ MeV for $E_{lab} =$ 40 - 80 MeV ; $R_j = R_{cr} = 0.73\ (20^{1/3} + 27^{1/3})$ fm and $V_j = V_{cr} = -73.08$ MeV for $E_{lab} \geqslant 120$ MeV. Calculations using the Glas-Mosel model[28] with these parameters and a barrier width $\hbar\omega = 12$ MeV reproduced fairly well the whole excitation curve as shown in Fig.3. The parameters V_B and R_B are the height and position of the s-wave potential barrier, whereas R_{cr} and V_{cr} are the critical radius and the potential at this distance.[27,28] The average height of the interaction barrier obtained from the optical model fits of the elastic scattering data, $V_B = 19.1 \pm 0.04$ MeV, as reported in Table III, is consistent with the value from the Glas-Mosel model, whereas the average position, $R_B = 1.58 \pm 0.04\ (20^{1/3}+27^{1/3})$fm is slightly larger. Similar results were obtained with the proximity potential having $r_o = 1.35$ fm in Eq.(11) : $V_B = 19.4$ MeV, and $R_B = 1.54\ (20^{1/3} + 27^{1/3})$ fm. In light of the fits displayed in Fig. 3, this proximity potential can provide an acceptable description of the ion-ion interaction in the theoretical interpretation of the deeply inelastic collisions at 151 MeV, discussed in the next section.

The higher energy fusion cross sections are also compared to the predictions of the "statistical yrast line" model,[29] based on the formula

$$\sigma_{fus} = (\pi I_c / \mu) \left[1 + (Q - \Delta Q) / E \right], \qquad (14)$$

where I_c is the compound nucleus moment of inertia assumed to be equal to that of a spherical rigid body of radius $R = r_o A_c^{1/3}$; and E are the reduced mass and c.m. energy of the entrance channel, respectively ; Q is the Q value for the formation of the compound nucleus in its ground state ; and ΔQ is an additional energy to the yrast line. The basic assumption of this model is that heavy ions do not fuse at the usual yrast line of the compound nucleus where the nucleon temperature is $T = 0$, and the level density low ; fusion occurs if the system lies on or above the "statistical yrast line" in a region with $T > 0$ and high level density. The statistical yrast line is assumed then to run parallel to the yrast line with an additional energy ΔQ.

Most of the experimental cross section for systems up to $A_1 + A_2 = 80$ could be fitted by Lee et al.[29] using Eq.(14) with the parameters $r_o = 1.20 \pm 0.05$ fm and $\Delta Q = 10 \pm 2.5$ MeV. Some experimental data, however, such as those on the $^{16}O + {}^{27}Al$ system, do not follow the systematics of this model. Lee et al.[26] in a later work shown that in fact their own measurements agree with the predictions from the statistical yrast line model, calculated with $r_o = 1.22$ fm and $\Delta Q = 10$ MeV. The discrepancy of these predictions with the data at the highest energy is attributed by the authors to the underestimate of the fusion cross section in Kozub et al.[18] measurements which excluded high Z nuclei at energies ≥ 15 MeV from the fusion yields.

Fig.3 shows a similar situation for the $^{20}Ne + {}^{27}Al$ system. The high energy part of the fusion cross section, including the present measurements and other available data,[18-20] falls off, in function of increasing energy, faster than the predictions from the statistical yrast line model using the same parameters as for $^{16}O + {}^{27}Al$.[26] Variations on the parameters within the standard deviation indicated by Lee et al.[29] could not eliminate these discrepancies.

C - DEEPLY INELASTIC COLLISIONS

The kinetic energies of the deeply inelastic fragments reflect the scission configuration of the dinuclear complex, which may be approximately described by two uniform spheres of radii R_3 and R_4 joined by a thin neck. The mass centers of the two spheres are then separated by a distance

$$d = R_3 + R_4 + \delta \ , \tag{15}$$

where δ is the neck length and R_i is about $R_i = 1.2\ A_i^{1/3}$ fm.

The total kinetic energy of the rotating dinuclear system at scission is

$$E_F = V_{Coul}(d) + V_{nucl}(d) + F^2 \frac{l_i(l_i+1)\hbar^2}{2\mu_f d^2} , \tag{16}$$

where μ_f is the reduced mass of the exit channel, F the ratio of the exit channel angular momentum to the entrance channel angular momentum l_i. In classical friction models this ratio for a scission configuration with rigid rotation is given by[52]

$$F = \mu_f d^2 / (\mu_f d^2 + I_3 + I_4) \tag{17}$$

where I_3, I_4 are the moments of inertia of the separated fragments,

$$I_i = \frac{2}{5} m_i R_i^2 , \tag{18}$$

m_i being the fragment mass.

On light systems the centrifugal barrier in Eq.(16) is comparable to the Coulomb one, so that the rotation of the complex plays a significant role in the behaviour of the kinetic energy.An unambiguous assessment of the rotational contribution in Eq.(16) requires an exact knowledge of l_i, d and the nuclear potential at d.

In their analysis of ^{20}Ne + ^{27}Al data at 120 MeV, Natowitz et al.[19] assumed that the deeply inelastic collisions arise for any detected fragment from a fixed angular momentum chosen to be just above those leading to fusion. With V_{nucl} taken from Bass[48], they have solved Eq.(16) for the scission distance which was found to be 10.2 fm for the symmetric division. Braun-Munzinger et al.[49] have pointed out the ambiguities in such a determination of the rotational energy based on measurements of the fragment energies at a single bombarding energy. These ambiguities can be, nevertheless,removed when the dependence of the final channel kinetic energy on beam energy is analyzed. Such an analysis[49] performed by the authors for ^{35}Cl + ^{27}Al led to a large scission distance as in Natowitz et al.[19] Betts and DiCenzo[30] reanalyzing the data for $^{20}Ne + ^{27}Al$ and $^{35}Cl + ^{27}Al$ assumed that scission effectively occurs at the critical distance $d = R_{cr} = 1.0\ (A_1^{1/3} + A_2^{1/3})$ fm, so that the nuclear potential V_{cr} at this distance can be deduced from the fusion data.[27,28] They demonstrated that, in fact, equally consistent methods of analysis can lead to quite different values for the scission radius and concluded that a study of Eq.(16) alone is insufficient for an unambigous determination of the final fragment energies.

Indeed Eq.(16) can be satisfied either by a solution with d much larger than the nuclear radii so that the nuclear potential is practically negligible or by a solution with d comparable to the nuclear radii where the increases of the Coulomb and rotational parts can be compensated for by the attractive nuclear potential. In a recent study[16] of the system $^{20}Ne + ^{40}Ca$, it was suggested that these two solutions correspond to the two physical components of the deeply inelastic collision : a fast interaction time and partly damped component at forward angle, and a fully damped component at backward angle. The fully damped component is associated with a large overlap between the colliding nuclei, i.e. with a small impact parameter. It is reasonable to assume then that the deeply inelastic collisions arise from a few incident partial waves just larger than those leading to fusion as in previous analyses[19,49,50]. The partly damped component near the grazing angle is associated with a large scission distance. Since the dynamic equilibrium is not established, the kinetic energy damping should depend on the amount of nucleon transfer which is related to the initial impact parameter, i.e. on the degree of overlap between the interacting nuclei in the initial stage of the reaction. It may be thus assumed that the deeply inelastic transfer reaction is associated with a small number of partial waves centered at

$$l_i = \alpha l_{cr} + (1 - \alpha)\, l_{gr}\ , \qquad (19)$$

where α accounts for the degree of nuclear overlap, l_{cr} and l_{gr} are, respectively, the critical and grazing angular momenta. Eq.(19) does not include the contribution from the low angular momentum window predicted by the Time Dependent Hartree-Fock Theory[4,5] but not yet experimentally confirmed.

Assuming that the nucleon transfer is proportional to the volume of one of the interacting nuclei which is swept by the other nucleus, Simbel and Abul-Magd[51] have shown that

$$\alpha = (N \ / N_{max})^{1/2}, \tag{20}$$

where N is the number of transferred nucleons and N_{max} is the maximum of this number corresponding to a maximum overlap and then to the initial angular momentum equal to l_{cr}. If it is assumed that l_{cr} corresponds to an overlap at the critical distance

$$R_{cr} = r_{cr} \ (A_1^{1/3} + A_2^{1/3}) \ , \tag{21}$$

and that the grazing occurs at

$$R_{gr} = r_{gr} \ (A_1^{1/3} + A_2^{1/3}), \tag{22}$$

N_{max} is approximately[51]

$$N_{max} = \frac{3}{4} A_1 \ (1 - \frac{r_{cr}}{r_{gr}})^2 \left[1 + (\frac{A_2}{A_1})^{1/3} \right]^2 . \tag{23}$$

The grazing distance R_{gr} can be deduced from the quarter-point angle $\theta_{1/4}$ of the elastic scattering angular distribution through the classical relationship

$$R_{gr} = \frac{\eta}{k} (1 + \frac{1}{\sin\frac{1}{2} \theta_{1/4}}) \tag{24}$$

where η and k are the Sommerfeld parameter and the wave number, respectively.

With $\theta_{1/4} = 16°$, as reported in Table III,

$$R_{gr} = 1.55\ (20^{1/3} + 27^{1/3}) = 8.85\ \text{fm}. \qquad (25)$$

With the critical radius deduced from the available fusion data through the Glas-Mosel model, $r_{cr} = 0.73$ fm, the maximum number of transferred nucleon is then $N_{max} = 18.6$. If a standard value $r_{cr} = 1$ fm is used, $N_{max} = 8.4$. This latter value is more consistent with the experimental results, since the fragments with $N > 8$, such as Be and B are essentially produced by a fully equilibrated system : their angular distributions are very close to a $1/\sin\theta_{c.m.}$ picture, their c.m. kinetic energies, and the width of their energy spectra practically independent of angle, as discussed in Section III. Thus a critical radius of 0.73 fm deduced from the fusion data in Fig.3 is probably too small, and more measurements at high energy are needed to clarify this point. A similar conclusion has been drawn by Lee et al.[26] in their analysis of the $^{16}O + {}^{27}Al$ fusion data.[18,22-25]

In the following calculations, a r_{cr} of 1 fm was adopted, and then an N_{max} of 8.4 was used in Eq.(20). The initial angular momentum l_i was calculated through Eq.(19) with $l_{cr} = 38$ and $l_{gr} = 53$, deduced from the fusion and elastic scattering data, respectively. The nuclear potential in Eq.(16) was the proximity potential, with $r_o = 1.35$ fm in Eq.(11), obtained from the low-energy fusion data fit ; the mass and charge dependence of the nuclear potential is accounted for in the determination of the proximity potential parameters. It was assumed that the fragment mass is twice its charge, except for Be considered to be ^{9}Be. A point-charge potential was used for the Coulomb part, $V_{coul}(d) = Z_3\ Z_4\ e^2\ /d$. The only parameter to be varied in the calculations of the total kinetic energies E_f was then the neck length δ defined in Eq.(15).

Calculations with $\delta = 3.7$ fm, corresponding to an elongated dinuclear complex whose mass centers are separated by a distance of 10.5 fm, are compared in Fig.8 to the data at 12°. The data at the grazing angle,

θ_{gr} = 9.5° lab, cannot be used since the damped component is then dominated by the strong quasielastic component, particularly for the fragments near the projectile. With an angular momentum dependence deduced from Eq.(19) the calculations, represented by the dashed line, yield a maximum at the projectile charge Z = 10, while the experimental distribution is centered around Z = 9. Such a shift is understandable in terms of particle decay from the excited fragments prior to the detection. The kinetic energy calculated with Eq.(16) should then be corrected for the kinetic energy lost by the fragments through the evaporation process.

If the recoil effect is neglected, the postevaporation kinetic energy of the detected fragment is

$$E_3' = \frac{m_3 - \Delta m_3}{m_3} E_3 \tag{26}$$

where m_3 and E_3 are the mass and energy of the primary fragment and Δm_3 is the mass loss. The postevaporation total kinetic energy is then related to the energy calculated in Eq.(16) by

$$E_F' = E_F \left(1 - \frac{\Delta m_3}{m_3} \right) / \left(1 - \frac{\Delta m_3}{m_c - m_3} \right) \tag{27}$$

where m_c is the composite system mass.

The kinetic energy correction imply then the calculation of the average number of particles evaporated by the fragment before detection. Assuming that the total excitation energy is divided between the fragments in the ratio of their masses, an iterative procedure using an evaporation code and Eq.(27) may, in principle, be used to fit the experimental data.[19,52] In the present work the excitation energy of the projectilelike fragments is about 10 - 30 MeV. Such energies are not far above the threshold for production of nucleons and alpha particles so that the average number of particles evaporated depends appreciably on both the charge and the mass of the fragment. Measurements of the charge distribution alone is not sufficient for an accurate determination of the decay mass Δm_3.

A rough estimate of Δm_3 can, however, be made by assuming that the outcoming fragment looses its excitation energy down to the particle threshold at about 10 MeV by evaporating nucleons which take off roughly 10 MeV each.[53] The average number of evaporated nucleons by a primary fragment is then

$$\Delta m = (E_{exc} - 10) / 10 \qquad (28)$$

where E_{exc} is the excitation energy in MeV. Calculations with the evaporation code EVA[54] confirm the simple estimate in Eq.(28) to within 30 %.

The particle decay corrections using Eqs.(27) and (28) lead to the solid line curve in Fig.8 (upper), which is in qualitative agreement with the data when the number of transferred nucleons N is smaller than the maximum N_{max} = 8.4. For fragments with $N > N_{max}$, an overlap factor $\alpha = 1$ was assumed in the calculations. In fact their production is governed by a fully equilibrated system, as discussed precedingly.

Similarly, the angular behavior of the experimental cross section and kinetic energy shown in Figs. 6 and 7 suggest a fully equilibrated process for the fragment production at angles backward of 30°. In order to minimize the accidental uncertainties, average values of the kinetic energy between 30° and 40° are plotted in the lower part of Fig.8. The calculations were performed with δ=-0.5 fm, that corresponds to an interaction distance of $1.1\ (20^{1/3} + 27^{1/3})$ fm. The angular momentum l_i before scission was kept fixed to $l_{cr} + 1 = 39$. Particle decays of the primary fragments were also corrected for using Eqs.(27) and (28). The data are then well reproduced by these calculations based on a fully equilibrated dinuclear complex formed by a maximum overlap of the colliding nuclei in the initial stage. The mass centers of the dinuclear complex are then separated by a distance of 6.5 fm instead of 10.5 fm obtained for the elongated configuration leading to the fast component.

V. SUMMARY AND CONCLUSION

The collision of ^{20}Ne on ^{27}Al was studied by measuring cross sections of complete fusion, elastic scattering and deeply inelastic reactions.

The average trend of the fusion excitation curve can be easily fitted by the Glas-Mosel model calculations to deduce the s-wave interaction barrier and the critical parameters. The high energy part is in notable discrepancy with predictions from the statistical yrast line model. However no definite conclusion can be drawn since a critical radius of 0.73 fm deduced from the data presently available is probably too small and more measurements at high energy are needed to clarify this point.

Angular distributions of the deeply inelastic products were measured at 151 MeV for fragments from Be to Mg. Although the ^{20}Ne+^{27}Al system is relative light, the main features of the data are similar to those observed for heavier systems. The fragment total kinetic energy were interpreted with a model based on the scission of a rotating dinuclear complex whose contributing initial angular momentum depends explicitly on the amount of nucleon transfer. The production of the Be, B, and Mg fragments is determined essentially by a fully equilibrated dinuclear complex whose components are separated by a distance close to the fusion critical distance. The rotational energy contribution to the fragment kinetic energy is determined by the angular momentum just greater than l_{cr}. Such a process is also present in the production of the fragments closer to the projectile, but it competes at angles around the grazing one with a fast interaction time process governed by the formation of an elongated dinuclear complex having a neck length of about 3.7 fm. The amount of transferred nucleons depends then on the initial angular momentum of the colliding nuclei, which determines their degree of overlap through their initial impact parameter. A qualitative understanding of the fragment production in the deeply inelastic collisions was obtained through the present crude approach.

The authors would like to thank A. Maurice for his technical assistance, and J.P. Richaud for the target preparation.

References :

1) ... J.M. ...der, and G.R. Satchler, Phys. Rep. 69, 374 (1981) and references therein.

2) U. Mosel, in Proceedings of the 3rd Adriatic Europhysics Study Conference on the Dynamics of Heavy-Ion Collisions, Hvar, Yougoslavia, 1981, edited by N. Cindro, ...cci, and W. Greiner (North Holland Publishing Company, Amsterdam, 1981). p.1.

3) J.R. Huizenga, J.R. Birkelund, W.U. Schröder, W.W. Wilcke, and H.J. Wollersheim, in Proceedings quoted in Ref. 2, p.15.

4) M.S. Weiss, in Proceedings quoted in Ref. 2, p. 115.

5) ... Irvine, J. Phys. G. : Nucl. Phys. 7, 1671 (1981).

6) K.R.S. Devi, A.K. Dhar, M.R. Strayer, Phys. Rev. C23, 2062 (1981).

7) V.V. Volkov, Phys. Rep. 44, 93 (1978).

8) M. Lefort and Ch. Ngô, Ann. Phys. (Paris) 3, 5 (1978).

9) C.K. Gelbke, D.K. Scott, M. Bini, D.L. Hendrie, J.L. Laville, J. Mahoney, M.C. Mermaz, and C. Olmer, Phys. Lett. 70B, 415 (1977).

10) H. Fröhlich, T. Shimoda, M. Ishihara, K. Nagatani, T. Udagawa, and T. Tamura, Phys. Lett. 42, 1518 (1979).

11) T. Udagawa, T. Tamura, T. Shimoda, H. Fröhlich, M. Ishihara, and K. Nagatani, Phys. Rev. C20, 1949 (1979).

12) K.W. McVoy and M.C. Nemes, Z. Phys. A295, 177 (1980)

13) Ch. Egelhaaf, G. Bohlen, H. Fuchs, A. Gamp, H. Homeyer, and H. Kluge, Phys. Rev. Lett. 46, 813 (1981).

14) Nguyen Van Sen, G. Ratel, R. Darves-Blanc, J.C. Gondrand, and F. Merchez, Phys. Rev. C17, 639 (1978).

15) Nguyen Van Sen, R. Darves-Blanc, J.C. Gondrand, and F. Merchez, Phys. Rev. C20, 969 (1979).

16) Nguyen Van Sen, J.C. Gondrand, F. Merchez, and R. Darves-Blanc, Phys. Rev. C22, 2424 (1980).

17) G. Madurga, A. Jadraque, and M. Lozano, Phys. Rev. C23, 1536 (1981)

18) R.L. Kozub, N.H. Lu, J.M. Miller, D. Logan, T.W. Debiak, and L. Kowalski, Phys. Rev.,C11, 1497 (1975).

19) J.B. Natowitz, M.N. Namboodiri, R. Eggers, P. Gonthier, K. Geoffroy, R. Hanus, C. Towsley, and K. Das, Nucl. Phys.,A277, 477 (1977).

20) W. Bohne, K. Grabisch, H. Morgenstern, and W. Stöffler, Proc. of the Int. Symposium onHeavy Ion Fusion Reactions, 1980,Bad Honnef,Germany(unpublished).

21) L. Kowalski, J.C. Jodogne, and J.M. Miller, Phys. Rev., 169, 894 (1968).

22) J. Dauk, K.P. Lieb, and A.M. Kleinfeld, Nucl. Phys.,A241, 170 (1975).

23) B.B. Black, R.R. Betts, C. Gaarde, J.S. Larsen, E. Michelsen, and Tai Kuang-Hsi, Nucl. Phys., A285, 317 (1977).

24) Y. Eisen, I. Tserruya, Y. Eyal, Z. Fraenkel, and M. Hillman, Nucl. Phys., A291, 459 (1977).

25) R. Rascher, W.F.J. Müller, and K.P. Lieb, Phys. Rev., C20, 1028 (1979).

26) S.M. Lee, Y. Higashi, Y. Nagashima, S. Hanashima, M. Sato, H. Yamaguchi, M. Yamanouchi, and T. Matsuse, Phys. Lett., 98B, 418 (1981).

27) J. Galin, D. Guerreau, M. Lefort, and X. Tarrago, Phys. Rev.,C9, 1018 (1974).

28) D. Glas and U. Mosel, Nucl. Phys., A237, 429 (1975).

29) S.M. Lee, T. Matsuse and A. Arima, Phys. Rev. Lett., 45, 165 (1980).

30) F.E. Obenshain, R.L. Ferguson, M.L. Halbert, D.C. Hensley, H. Nakahara, F. Plasil, F. Pleasonton, A.H. Snell, and R.G. Stokstad, Phys. Rev., C18, 764 (1978).

31) R.A. Dayras, R.G. Stokstad, D.C. Hensley, and M.L. Halbert, Phys. Rev. C22, 1485 (1980).

32) G.J. Mathews, J.B. Moulton, G.J. Wozniak, B. Cauvin, R.P. Schmitt, J.S. Sventek, and L.G. Moretto, Phys. Rev. C25, 300 (1982).

33) M.H. Simbel and A.Y. Abul-Magd, Z. Phys., A294, 277 (1980).

34) S. Cohen, F. Plasil, and W.J. Swiatecki, Ann.Phys.,(N.Y.)82, 557 (1974).

35) M. Blann, University of Rochester Report N° COO-3494-29, 1976 (unpublished).

36) F.G. Perey, Phys. Rev., 131, 745 (1963), and private communication.

37) G.R. Satchler, Phys. Lett., 58B, 408 (1975).

38) Nguyen Van Sen, R. Darves-Blanc, F. Merchez, and J.C. Gondrand, Z. Phys., A276, 335 (1976).

39) Nguyen Van Sen, J.C. Gondrand, F. Merchez, and R. Darves-Blanc, Nuovo Cim., 33A, 361 (1976).

40) S. Krewald, A. Djalocis, and S. Gopal, Phys. Rev., C24, 966 (1981).

41) J.G. Cramer and R.M. DeVries, Phys. Rev., C22, 91 (1980).

42) K. Siwek-Wilczynska and J. Wilczynski, Phys. Lett., 55B, 270 (1975) ; 74B, 313 (1978).

43) J.S. Blair, Phys. Rev., 108, 827 (1957).

44) D.L. Hill and J.A. Wleeler, Phys. Rev., 89, 1102 (1953).

45) J. Blocki, J. Randrup, W.J. Swiatecki, and C.F. Tsang, Ann. Phys., (N.Y.) 105, 427 (1977).

46) L.C. Vaz and J.M. Alexander, Phys. Rev., C18, 2152 (1978).

47) M.S. Chiou, M.W. Wu, N. Easwar, and J.V. Maher, Phys. Rev., C24, 2507 (1981).

48) R. Bass, Phys. Rev. Lett., 39, 265 (1977).

49) P. Braun-Munzinger, T.M. Cormier, and C.K. Gelbke, Phys. Rev. Lett., 37, 1582 (1976).

50) R.R. Betts and S.B. DiCenzo, Phys. Rev. C19, 2070 (1979).

51) M.H. Simbel and A.Y. Abul-Magd, Z. Phys., A294, 277 (1980).

52) T.M. Cormier, P. Braun-Munzinger, P.M. Cormier, J.W. Harris, and L.L. Lee, Jr., Phys. Rev., C16, 215 (1977).

53) P. Wastyn, H. Feldmeier, F. Beck, M. Dworzecka, H. Genz, M. Mutterer, A. Richter, G. Schrieder, and J.P. Theobald, Nucl. Phys., A332, 455 (1979).

54) Y. Eyal, M. Beckerman, R. Chechik, Z. Fraenkel, and H. Stocker, Phys. Rev., C13, 1527 (1976).

TABLE I - Experimental fusion cross sections and critical fusion angular momenta.

E_{lab}(MeV)	σ_{fus}(mb)	l_{cr}($\hbar$)
32.5	125 $\pm$ 10	5
41.5	450 $\pm$ 35	13
50	712 $\pm$ 60	18
55.7	823 $\pm$ 40	20
63	1044 $\pm$ 70	25
70	1090 $\pm$ 70	27
100	1230 $\pm$ 60	35
151	1007 $\pm$ 50	38

TABLE II - Energy- and angle-integrated elemental cross section for deeply inelastic fragments produced in the $^{20}Ne + ^{27}Al$ collision at 151 MeV.

Fragment	Yield(mb)	Fragment	Yield(mb)
Be	12 ± 2	F	195 ± 30
B	35 ± 3	Ne	$<250 \pm 50$
C	130 ± 13	Na	100 ± 10
N	105 ± 11	Mg	90 ± 9
O	315 ± 50	Total	1230 ± 180

TABLE III - Optical model parameters[a] for $^{20}Ne + ^{27}Al$. Also reported are the total reaction cross sections σ_R deduced from the elastic scattering fits, the fusion cross section σ_{fus}^{OM} calculated from the real part of the optical potential, the height V_B^{OM} and position $r_B^{OM} = R_B^{OM}/(20^{1/3} + 27^{1/3})$ of the interaction barrier[b], the grazing angular momenta l_{gr} deduced from the c.m. quarter-point angle $\theta_{1/4}$, and the classical total reaction cross sections $\sigma_R^{(1/4)}$.

E_{lab}(MeV)	r_o(fm)	a(fm)	σ_R(mb)	σ_{fus}^{OM}(mb)	V_B(MeV)	r_B(fm)	$\theta_{1/4}$(deg)	l_{gr}(ħ)	$\sigma_R^{(1/4)}$(mb)
55.7	1.170	0.671	1274	956	19.06	1.59	52.7	25	1207
63	1.163	0.675	1441	1082	19.12	1.58	44.3	28	1328
125	1.190	0.687	2147	1273	18.67	1.62	19	49	1990
151	1.095	0.728	2035	762	19.60	1.53	16	53	1921

[a] With V = 56.86 MeV (see text) and W = 45 MeV. The energy-averaged radius and diffuseness are $\langle r_o \rangle = 1.15 \pm 0.04$ fm and $\langle a \rangle = 0.69 \pm 0.03$ fm.

[b] Energy-averaged values $\langle V_B \rangle = 19.1 \pm 0.4$ MeV and $\langle r_B \rangle = 1.58 \pm 0.04$ fm.

Figure captions :

FIG. 1. Typical examples of energy-integrated elemental yields deduced from the ionization chamber E vs ΔE two-dimensional spectra.(a) projectile-like fragments produced from 151 MeV ^{20}Ne collision with ^{27}Al, detected at 14° by the gas counter run at high pressure (see text) ; the elastic scattering peak is taken off the spectra during the off-line data reduction.(b) evaporation residues ($16 \leq Z \leq 23$) from the fusion of 63 MeV ^{20}Ne with ^{27}Al, detected at 10° by the gas counter run at low pressure.

FIG. 2. Typical angular distributions of the evaporation residue cross section for $^{20}Ne + {}^{27}Al$. The total fusion cross sections σ_{fus} is obtained by integrating the solid curve over angle. The most forward part not measured is deduced from the extrapolation procedure performed on the $d\sigma_{fus}/d\Omega$ angular distribution (see text).

FIG. 3. Fusion energy excitation curve for $^{20}Ne + {}^{27}Al$ including data from Kozub et al.[18], Natowitz et al.[19], Bohne et al.[20] and the present work. The solid line curve represents the Glas-Mosel model calculations with parameters V_B = 19.21 MeV, r_B = 1.44 fm, V_{cr} = -73.08 MeV, and r_{cr} = 0.73 fm. The dashed line : calculations with the barrier penetration model using the proximity potential with r_o = 1.35 fm. The dash and-dotted straight line (marked s.y.) : statistical yrast model predictions using the parameters obtained by Lee et al.[26] for $^{16}O + {}^{27}Al$, r_o = 1.22 fm and ΔQ = 10 MeV.

FIG. 4. Elastic scattering angular distributions for $^{20}Ne + {}^{27}Al$ compared with best-fit optical model calculations using parameters in Table III.

FIG. 5. Bell-shaped energy spectra for fragments from Be to Al produced by the $^{20}Ne + ^{27}Al$ collision. Typical statistical error bars are plotted. The solid lines are drawn to guide the eye. At 8° the spectra are not shown for Be, B, and C since their shape is nearly independent of angle, whereas no clear bell-shaped structure can be observed for Ne (see text).

FIG. 6. Angular distributions of the bell-shaped part of the spectra. The dashed curves are deduced from a $1/\sin\theta_{c.m.}$ angular distribution, using two-body kinematics and the most probable Q values ; the curves are normalized to the data at 30°.

FIG. 7. Total kinetic energies of the fragment exit channel in the center-of-mass system.

FIG. 8. Total kinetic energies of the fragments detected at 12° and angle-averaged values between 30° and 40°. The solid (dashed) lines are calculations based on a rotating dinuclear model with (without) corrections for particle decay from the excited primary fragments.

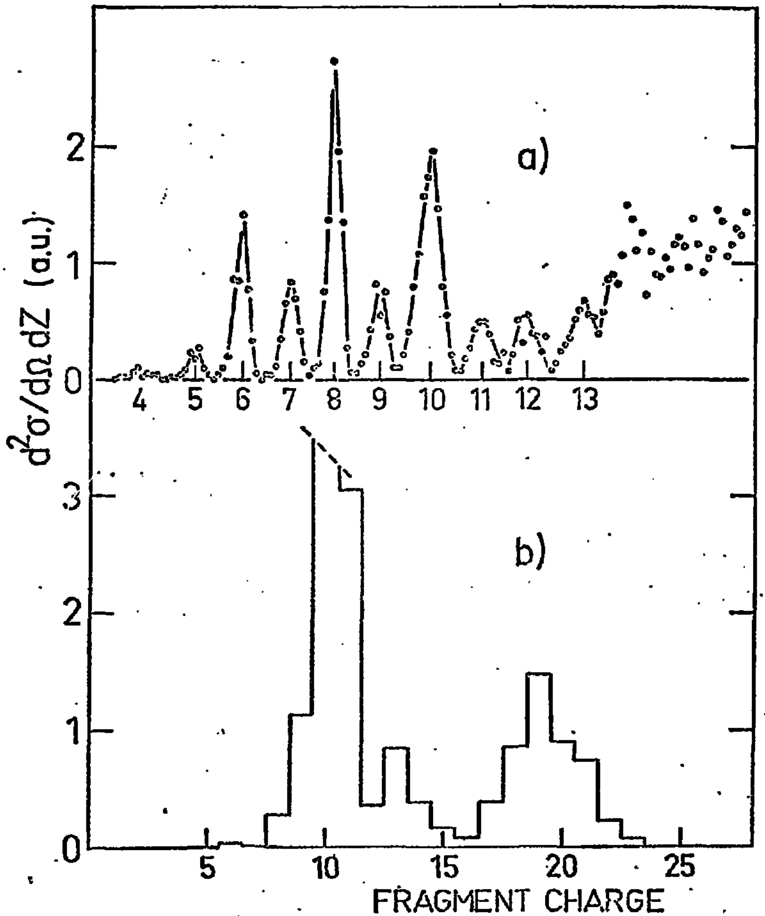
a)
b)
$d^2\sigma/d\Omega dZ$ (a.u.)
0
1
2
3
4
5
6
7
8
9
10
11
12
13
15
20
25
FRAGMENT CHARGE

FIG. 1

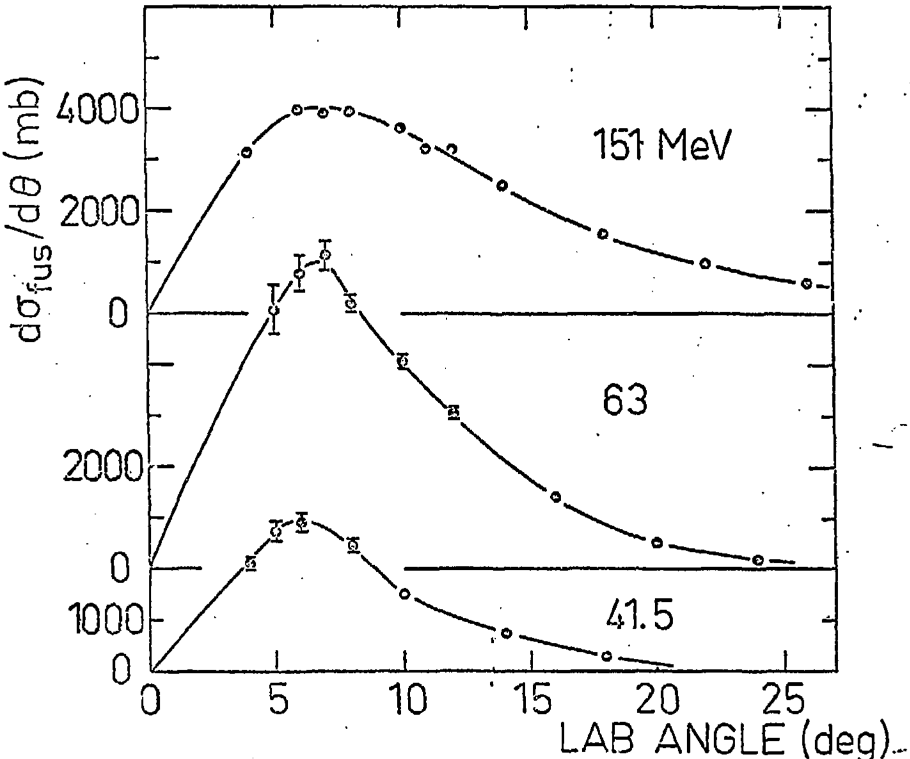

$d\sigma_{fus}/d\theta$ (mb)
4000
2000
0
2000
0
1000
0
151 MeV
63
41.5
0
5
10
15
20
25
LAB ANGLE (deg)

FIG. 2

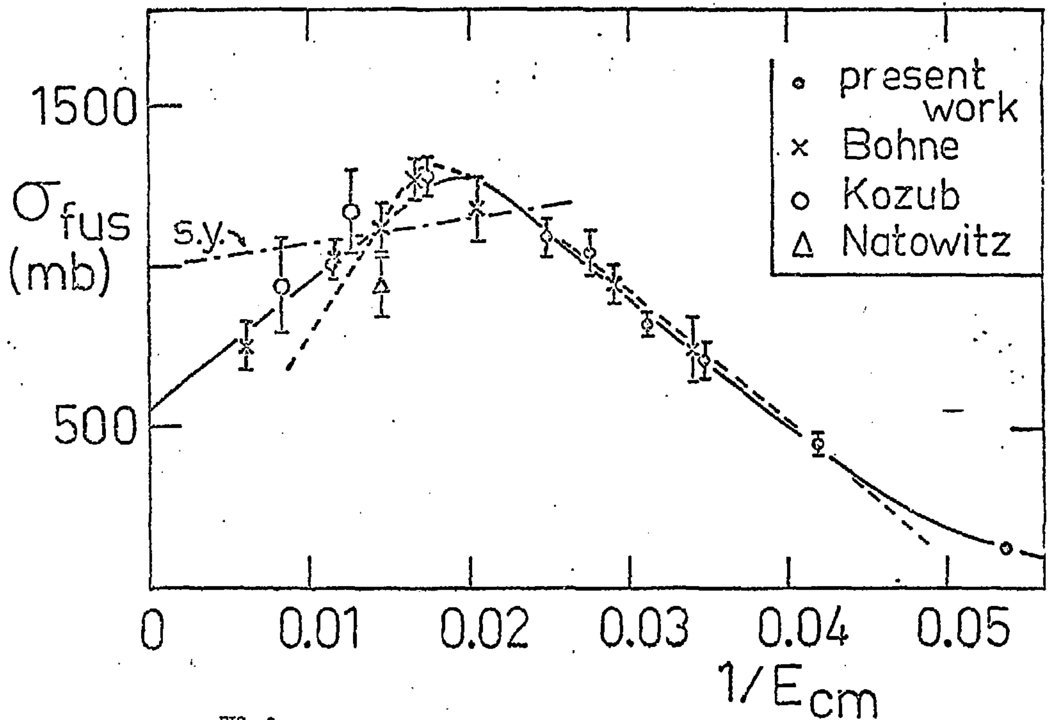
present work
Bohne
Kozub
Natowitz
1500
500
σfus (mb)
s.y.
0
0.01
0.02
0.03
0.04
0.05
1/Ecm

FIG. 3

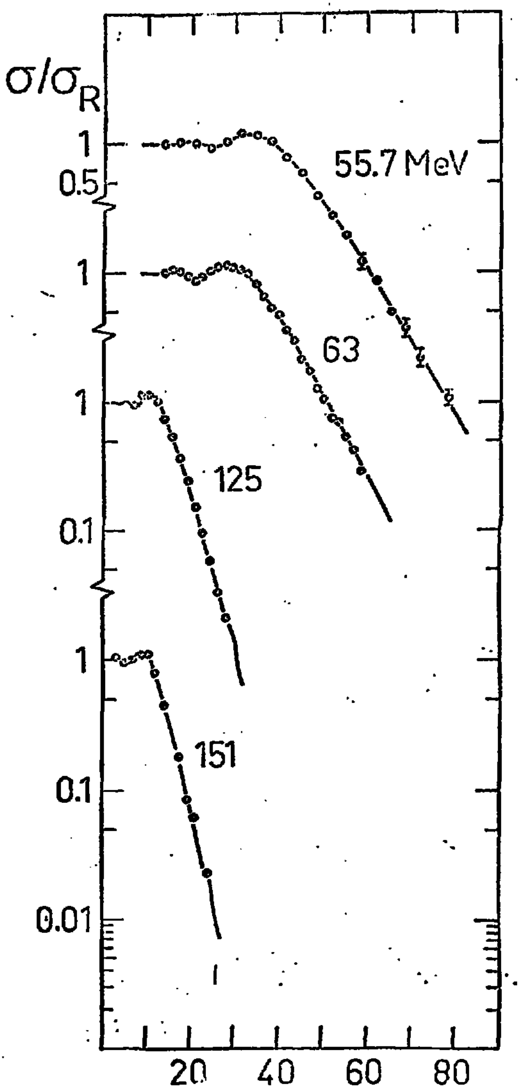

FIG. 4

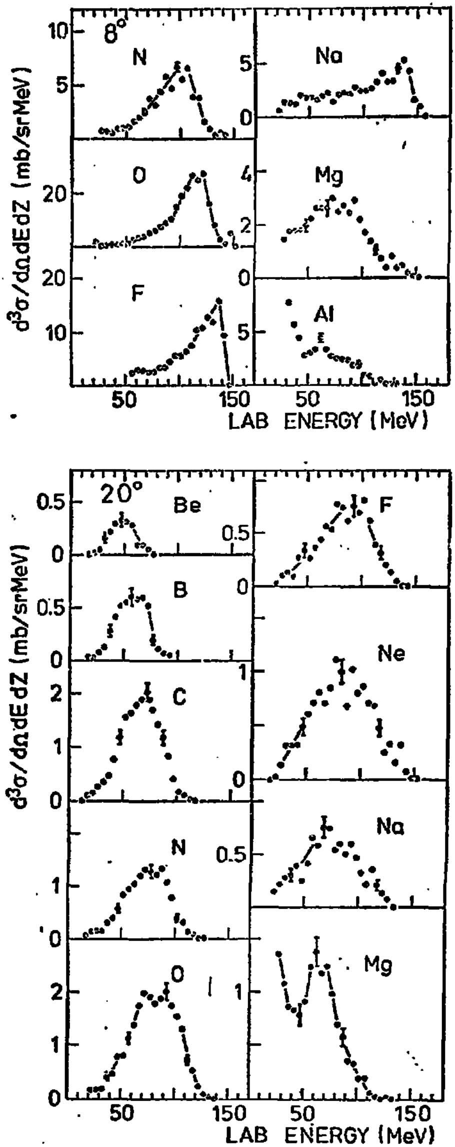
8°
N
O
F
Na
Mg
Al
d³σ/dΩdEdZ (mb/srMeV)
LAB ENERGY (MeV)
20°
Be
B
C
N
O
F
Ne
Na
Mg
d³σ/dΩdEdZ (mb/srMeV)
LAB ENERGY (MeV)

FIG. 5

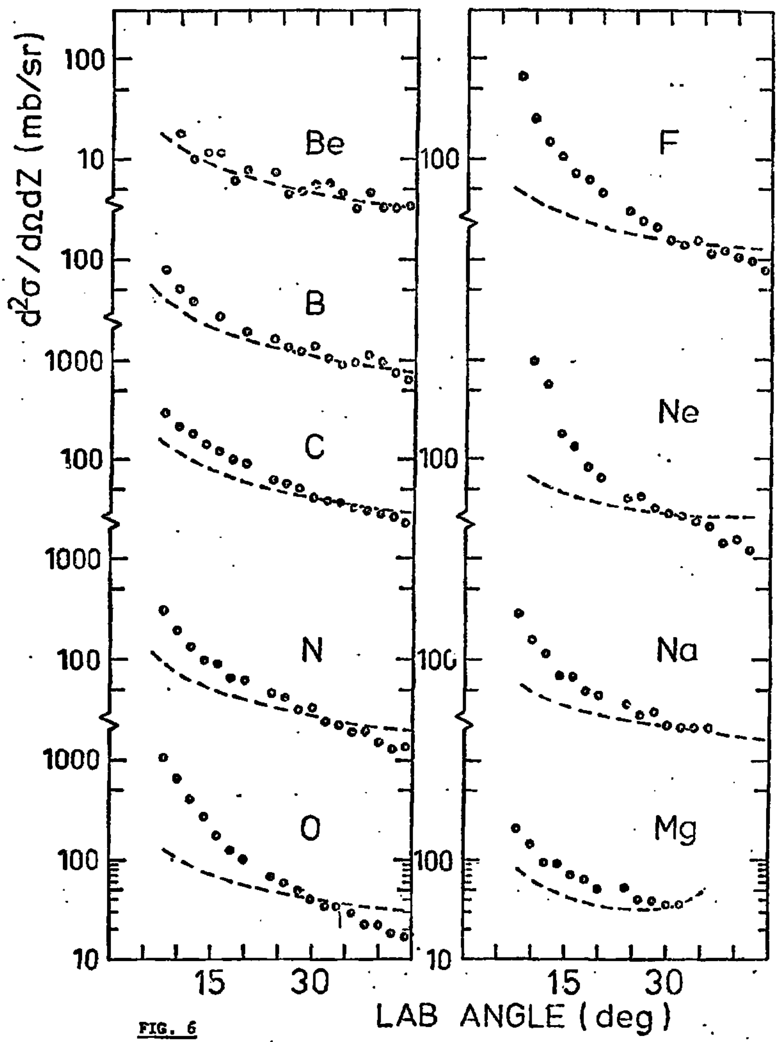

d²σ/dΩdZ (mb/sr)
Be
B
C
N
O
F
Ne
Na
Mg
100
10
100
1000
100
1000
100
1000
100
10
100
100
100
100
10
15
30
15
30
LAB ANGLE (deg)

FIG. 6

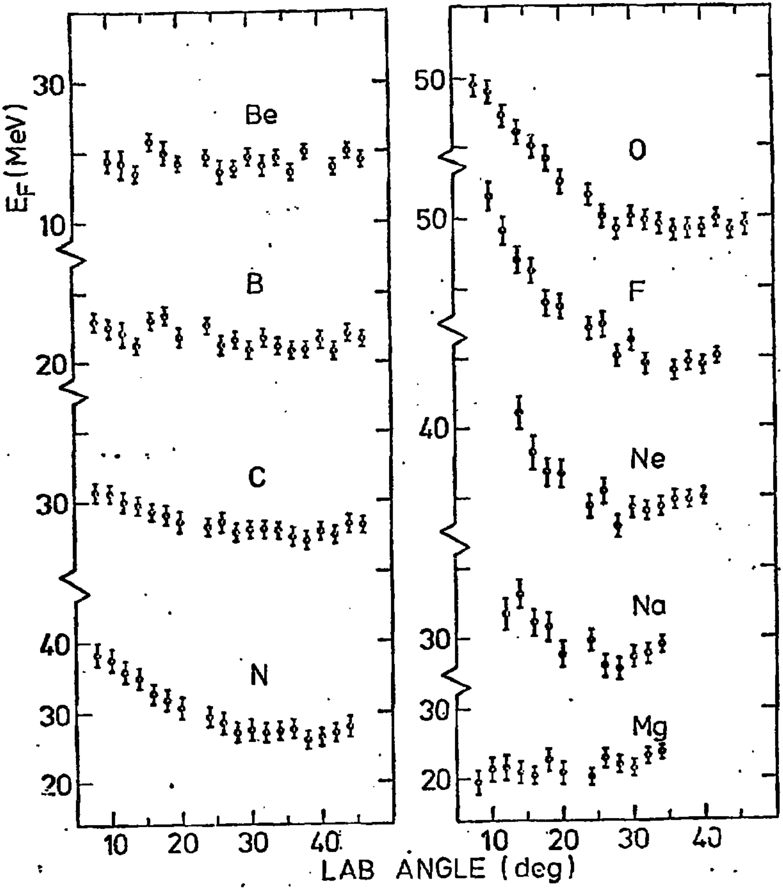

E_F (MeV)
Be
B
C
N
O
F
Ne
Na
Mg
30
10
20
30
40
30
20
50
50
40
30
30
20
10
20
30
40
10
20
30
40
LAB ANGLE (deg)

FIG. 7

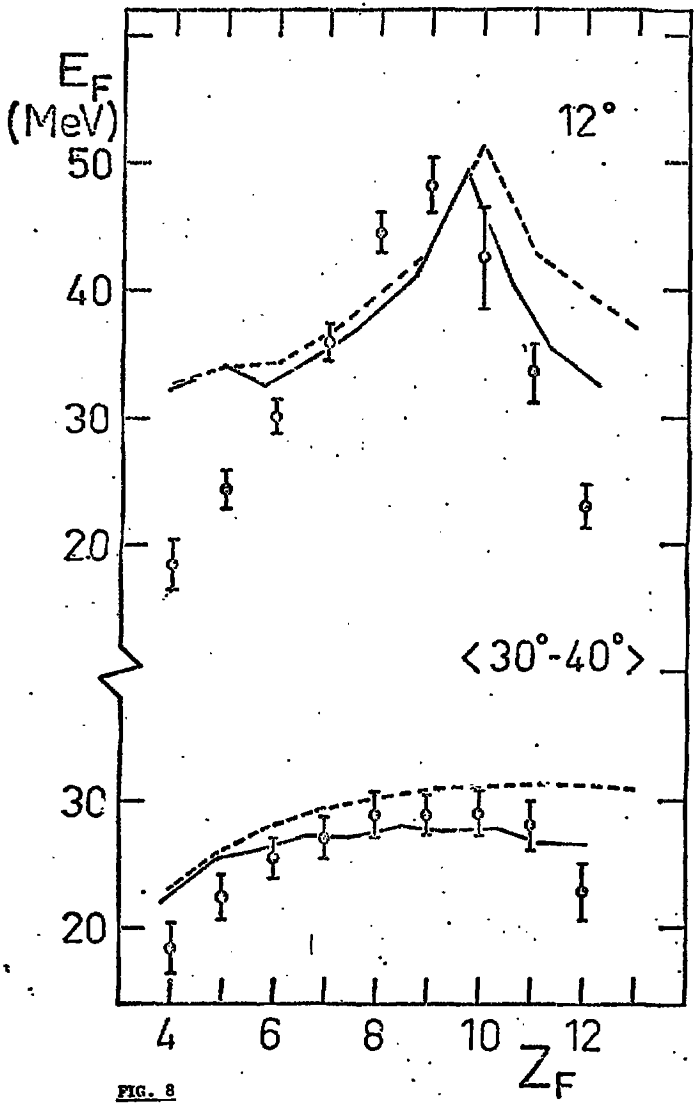

FIG. 8